

RESEARCH ARTICLE | AUGUST 15 2023

# Arbitrary wavefront uncertainty evaluation for the Shack–Hartmann wavefront sensor using physical optics propagation

Jichong Zhou ; Qiaozhi He ; Yuan Qu ; Dineng Zhao ; Ziyin Wu ; Jiamiao Yang  *Appl. Phys. Lett.* 123, 071102 (2023)<https://doi.org/10.1063/5.0163112>

CrossMark

## Articles You May Be Interested In


Completing the dark matter solutions in degenerate Kaluza-Klein theory

*J. Math. Phys.* (April 2019)

Gibbs measures based on 1d (an)harmonic oscillators as mean-field limits


*J. Math. Phys.* (April 2018)

An upper diameter bound for compact Ricci solitons with application to the Hitchin–Thorpe inequality. II

*J. Math. Phys.* (April 2018)


**The Beginner's Guide to Cryostats and Cryocoolers**  
A detailed analysis of cryogenic systems

[Download guide ▼](#)



# Arbitrary wavefront uncertainty evaluation for the Shack–Hartmann wavefront sensor using physical optics propagation

Cite as: Appl. Phys. Lett. **123**, 071102 (2023); doi: [10.1063/5.0163112](https://doi.org/10.1063/5.0163112)

Submitted: 16 June 2023 · Accepted: 3 August 2023 ·

Published Online: 15 August 2023



View Online



Export Citation



CrossMark

Jichong Zhou,<sup>1</sup> , Qiaozhi He,<sup>2</sup> , Yuan Qu,<sup>1,2</sup> , Dineng Zhao,<sup>3,4</sup> , Ziyin Wu,<sup>4</sup> , and Jiamiao Yang<sup>1,2,3,a)</sup>

## AFFILIATIONS

<sup>1</sup>School of Electronic Information and Electrical Engineering, Shanghai Jiao Tong University, Shanghai 200240, China

<sup>2</sup>Institute of Marine Equipment, Shanghai Jiao Tong University, Shanghai 200240, China

<sup>3</sup>Donghai Laboratory, Zhoushan, Zhejiang 316021, China

<sup>4</sup>Key Laboratory of Submarine Geosciences, Second Institute of Oceanography, Ministry of Natural Resources, Hangzhou 310012, China

<sup>a)</sup> Author to whom correspondence should be addressed: [jiamiaoyang@sjtu.edu.cn](mailto:jiamiaoyang@sjtu.edu.cn)

## ABSTRACT

The Shack–Hartmann wavefront sensor (SHWS) is a common option to characterize optical fields, due to its noninterference, high accuracy, and high-speed advantages. However, the current methods for evaluating measurement accuracy can only work for predefined standard wavefronts and cannot provide the error estimate for an arbitrary wavefront. Here, we propose an SHWS uncertainty evaluation approach for specific wavefronts based on the physical optics propagation. Our approach constructs a comprehensive SHWS model that incorporates twelve error sources. We analyzed the influence of different error sources on the measurement accuracy under the diffraction effect and reported that our model could achieve an accuracy of  $\lambda/559$  under the ideal condition. In the experiment, we measured three different wavefronts and confined their uncertainty down to  $\lambda/65$ ,  $\lambda/260$ , and  $\lambda/40$ , respectively. Our work may offer an effective solution for evaluating measurement errors in the high-accuracy wavefront measurement and provide a reliable, unbiased evaluation criterion.

Published under an exclusive license by AIP Publishing. <https://doi.org/10.1063/5.0163112>

Wavefront measurement techniques can quantify the phase distribution of optical field, which is critical in fields such as advanced manufacturing,<sup>1–4</sup> astronomy,<sup>5–8</sup> bioimaging,<sup>9,10</sup> and ophthalmology.<sup>11–13</sup> At present, the available techniques measuring wavefronts include phase-shifting interferometry,<sup>14–16</sup> shear interferometry,<sup>17–19</sup> point diffraction interferometry,<sup>20–22</sup> and the Shack–Hartmann wavefront sensor<sup>23</sup> (SHWS). Among them, the SHWS reconstructs the wavefront by dividing it into an array of sub-wavefronts. For each sub-wavefront, the local slope can be calculated according to the displacement of the associated focal spot.<sup>24</sup> As an alternative to interferometry, the SHWS possesses notable advantages. For example, it does not require a reference wavefront, eliminating the problems caused by the error of the reference wavefront itself. Instead, the SHWS can acquire the phase distribution of optical field in a single shot, making it simple and efficient.

The commercial SHWS can now achieve a nominal accuracy of  $\lambda/100$ ,<sup>25</sup> but this value is only valid for measuring a standard wavefront (plane or spherical wavefront). Since the error sources of the

SHWS have an inconsistent influence on different wavefronts, the declared nominal accuracy is inadequate for accurately characterizing measurement errors on an arbitrary wavefront. Recently, scholars have extensively analyzed and studied the structural errors,<sup>26,27</sup> detector errors,<sup>28–30</sup> algorithmic errors,<sup>31–39</sup> and calibration errors<sup>40,41</sup> in the SHWS error assessment. However, the previous studies often established an error transfer function considering only one or a few error sources existing in the SHWS measurement process. They are not comprehensive enough and omit the coupling between some error sources, resulting in compromised error analysis. The previous studies also neglected the influence of variability in the wavefront distribution on measurement accuracy. Hence, a high-accuracy measurement of an arbitrary wavefront by the SHWS requires a more comprehensive error assessment method than the previous ones.

Here, we propose an SHWS uncertainty evaluation approach to address the varying measurement accuracy issue encountered in the measurement of different wavefronts. In particular, using the physical optics propagation, we established an SHWS model covering 12 error

sources involving the sensor assembly, calibration, and measurement. Based on this model, a Monte Carlo program could estimate the measurement uncertainty for a specific wavefront. Compared with constructing an explicit error transfer function, our approach can investigate the influence of multiple error sources on the wavefront measurement accuracy at the diffraction scale and achieve a comprehensive assessment of measurement uncertainty of arbitrary wavefronts.

Figure 1 illustrates the principle of our proposed uncertainty evaluation approach based on the physical optics propagation. The SHWS model comprehends 12 common error sources related to the SHWS assembly, calibration, and measurement. Using the angular spectrum method, the model simulates the physical process of wavefront transmitting through a microlens array (MLA) and forming an array of focal spots on the CMOS sensor. After a centroid computation algorithm extracts the centroid positions of all the focal spots, we can accordingly calculate the spatial distribution of wavefront slopes and reconstruct the wavefront. Calculated from the reconstructed and measured wavefronts, the root mean square error (RMSE) represents the measurement error.

Figure 1(a) shows the physical optics propagation process of the SHWS. We employed Zernike polynomials to generate wavefronts with various distributions. The phase transfer function of the MLA can be constructed based on the principle of thin-lens approximation.<sup>42</sup> Subsequently, we employed the tilted-plane angle spectrum theory<sup>43</sup> to model the diffraction propagation process between the tilted planes of MLA and the CMOS sensor plane.

In the SHWS model, four types of errors are included: the installation error, image acquisition error, calibration error, and algorithmic error. The installation error results from the misalignment between the MLA and CMOS sensor during their installation, causing the three-dimensional angular deviations  $\delta_\alpha$ ,  $\delta_\beta$ , and  $\delta_\gamma$  [Fig. 1(a)]. The image acquisition error relates to many factors, such as the discrete sampling  $\delta_{\text{discrete}}$ , quantization  $\delta_{\text{quant}}$  and noise  $\delta_{\text{noise}}$ . The calibration error originates from the lack of strict alignment of SHWS [Fig. 1(b)]. During the calibration, the position and tilt angle of the incident wavefront are changed multiple times with respect to the coordinates defined by the MLA.<sup>41</sup> As a result, the deviations  $\delta_x$ ,  $\delta_y$ ,  $\delta_\theta$ , and  $\delta_\varphi$  emerge. The calibration errors can result in incorrect placement of

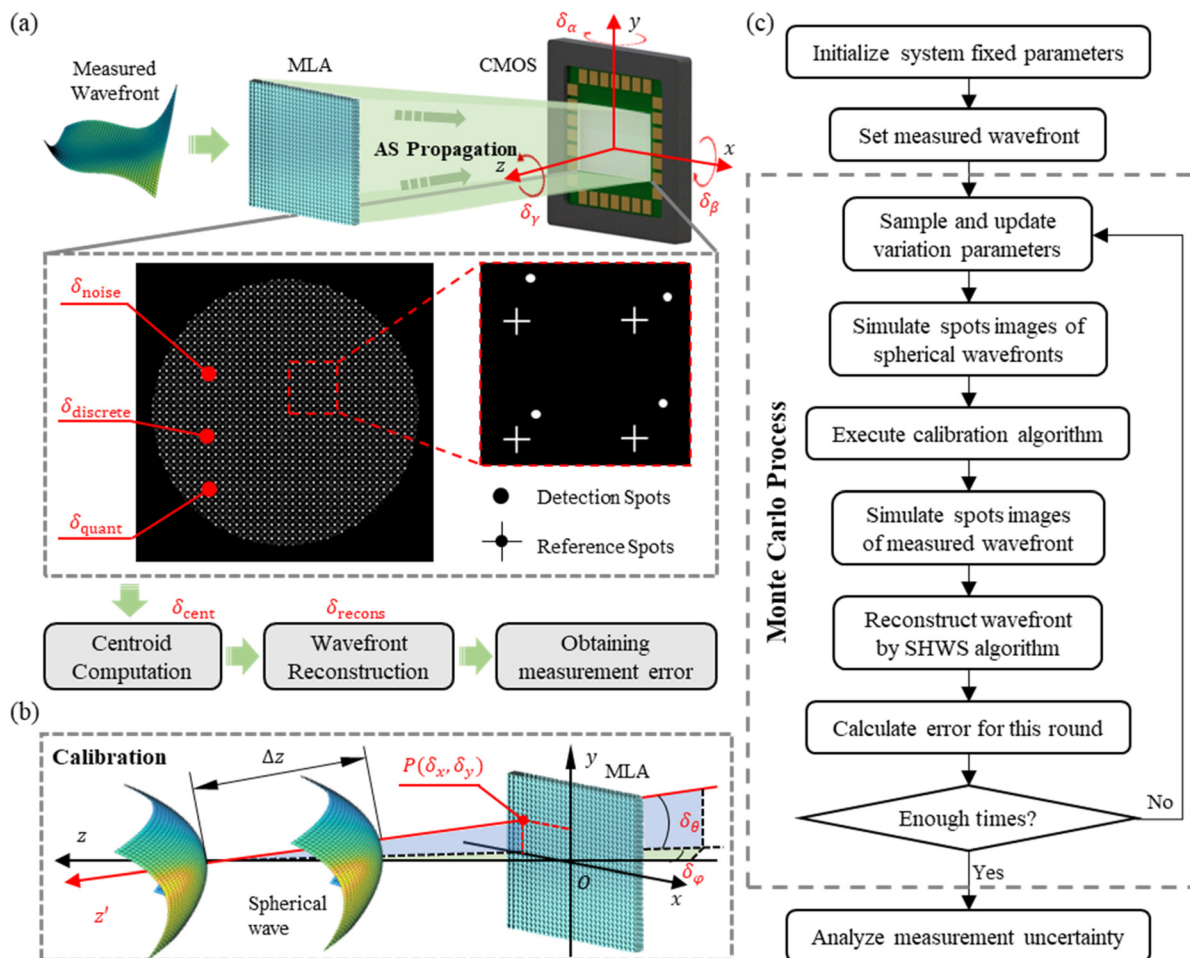


**FIG. 1.** Principle of the SHWS uncertainty evaluation approach. (a) Illustration of the SHWS error propagation model based on physical optics propagation. MLA, microlens array. AS, angular spectrum. (b) Schematic of SHWS spherical wavefronts calibration. (c) Flow chart for evaluating the uncertainty of SHWS for a measured wavefront using the Monte Carlo method. Variation parameters include installation errors ( $\delta_\alpha$ ,  $\delta_\beta$ , and  $\delta_\gamma$ ) and calibration errors ( $\delta_x$ ,  $\delta_y$ ,  $\delta_\theta$ , and  $\delta_\varphi$ ).

reference points, misestimation of distances between CMOS and MLA, and, therefore, a substantial increase in the total measurement error. The algorithmic errors comprise the centroid positioning error  $\delta_{\text{cent}}$  and wavefront reconstruction error  $\delta_{\text{recons}}$ .

Figure 1(c) illustrates the evaluation of measurement uncertainty of SHWS using the Monte Carlo method. First, the system's fixed parameters need to be initialized, including the MLA parameters (lenslet pitch, curvature, and numbers), CMOS sensor parameters (pixel size, resolution, and noise level), the distribution range of error sources, and the number of Monte Carlo cycles. Then, the measured wavefront is input, and the Monte Carlo loop begins. In each loop, the variation parameters, which consist of installation errors ( $\delta_x$ ,  $\delta_y$ , and  $\delta_z$ ) and calibration errors ( $\delta_\alpha$ ,  $\delta_\beta$ ,  $\delta_\gamma$ , and  $\delta_\phi$ ), are randomly sampled within their respective error ranges. Once the fixed system parameters and variation parameters are determined, multiple simulated spots images of spherical wavefronts with different curvatures are generated. The distance from the MLA to the CMOS sensor and the positions of reference points are then determined from these spots images by employing the spherical wavefronts calibration algorithm.<sup>41</sup> Subsequently, the spots image of the measured wavefront is simulated. The wavefront is reconstructed using the SHWS measurement algorithm, followed by a comparison with the measured wavefront to calculate the measurement error. If the predetermined number of loops has not been reached, the variation parameters are resampled, and the subsequent loop commences. Once the predetermined value is attained, the measurement uncertainty of the measured wavefront is determined by analyzing the measurement error values obtained throughout all the loops.

To verify our SHWS model, we analyzed the precision under the ideal plane wave calibration condition without any installation errors. In this case, the measurement error was ascribed exclusively to the algorithmic error and image acquisition error. The wavelength of our simulation is 632.8 nm, the assembly distance between CMOS and MLA is 5.2 mm, the lenslet pitch is 150  $\mu\text{m}$ , the radius of curvature of lens is 2.54 mm, the number of lenslets is  $39 \times 39$ , and the Zernike normalized diameter is 5.85 mm. Figure 2 illustrates the results of simulation for plane, spherical, and freeform wavefronts. Three wavefronts were selected for each type of wavefront for testing. The residual distribution shows that our model is able to reconstruct the wavefront with high accuracy. The plots at the bottom of Fig. 2 show the spatial distribution of measurement inaccuracies along the cross section of wavefronts. It can be seen that the maximum reconstruction error in the cross section remains under 2.2 nm.

Figure 3(a) depicts the measurement errors of the simulation model for 100 groups of plane, spherical, and freeform wavefronts at an average measurement error of 0.1, 0.3, and 1.6 nm, respectively. Obviously, the standard plane and spherical wavefronts had a measurement accuracy higher than the freeform wavefront, because the high-frequency components uniquely presented in the freeform wavefront led to a greater susceptibility to the inaccuracy of wavefront sampling. As a result, the highest measured error obtained for a spherical wavefront was taken as a reliable assessment of the SHWS model accuracy, which was 1.13 nm ( $\lambda/559$ ). The accuracy is limited by the SHWS paraxial approximation principle, structural parameters, and measurement algorithms. To enhance the accuracy of the model, one can employ strategies, such as increasing the focal length of MLA,

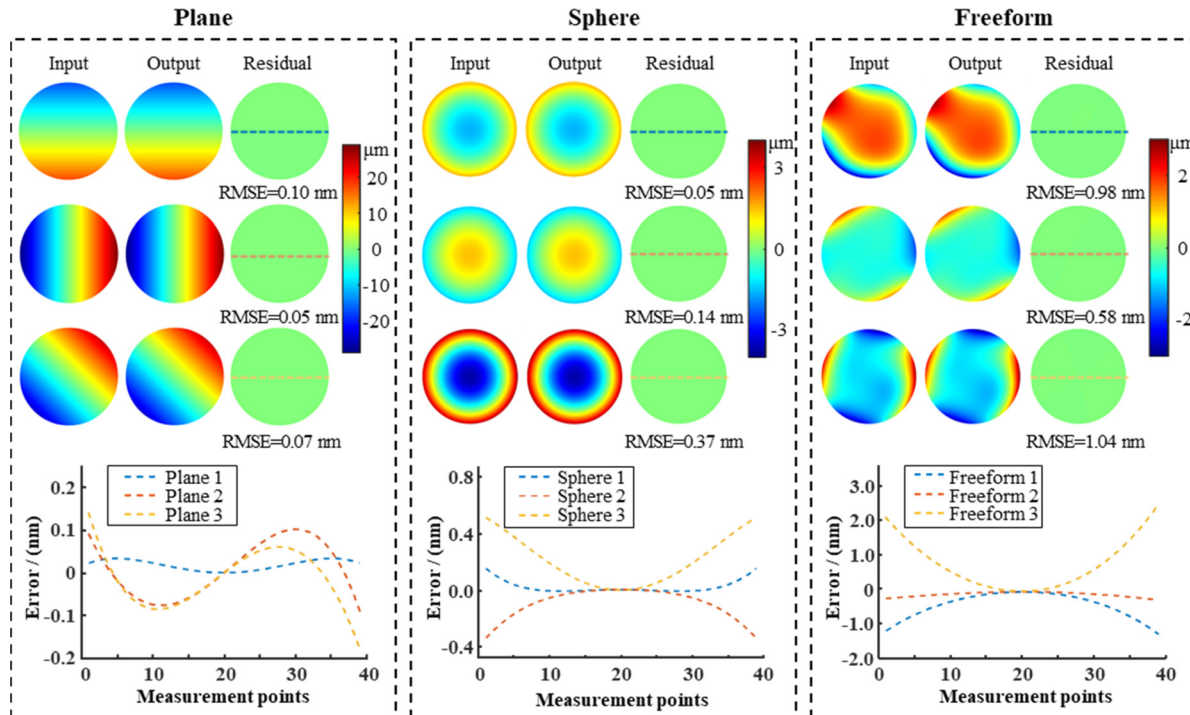
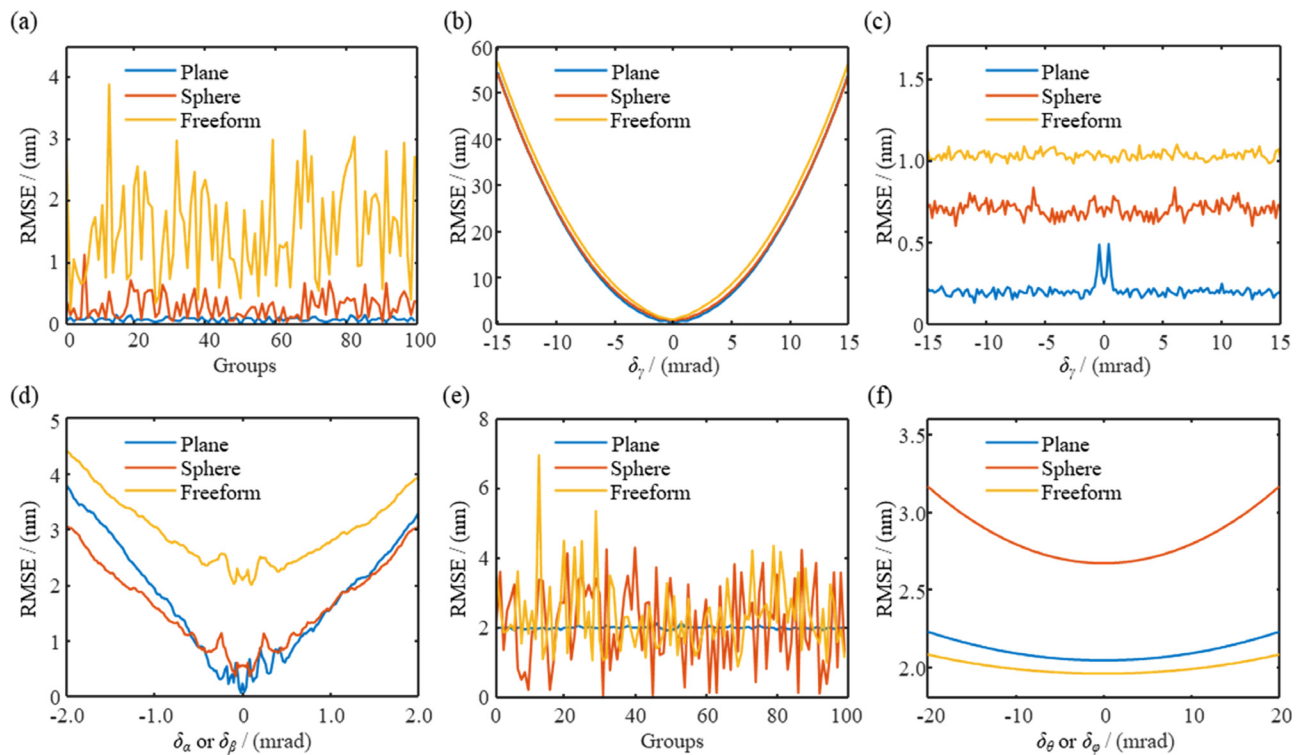


FIG. 2. SHWS simulation for plane, spherical, and freeform wavefronts. The residuals are represented in terms of RMSE. The corresponding error distribution along the dashed line in each residual map is shown at the bottom.





**FIG. 3.** Influence of different factors on the measurement accuracy. (a) Measurement error distributions based on the plane wavefront calibration. (b) Influence of  $\delta_\gamma$  on the measurement error. (c) Influence of  $\delta_\gamma$  on the measurement error after the rotation correction. (d) Influence of  $\delta_\alpha$  and  $\delta_\beta$  on the measurement error. (e) Measurement error distributions based on the spherical wavefront calibration. (f) Influence of  $\delta_\theta$  and  $\delta_\phi$  on the measurement error.

reducing the pitch between lenslets, and implementing more advanced SHWS measurement algorithms.

Figures 3(b)–3(d) show the effect of installation errors on the measurement accuracy. First, we found that an increase in the tilt angle  $\delta_\gamma$  resulted in a rise in the measurement error. Nevertheless, as this error causes only an image rotation, the rotation angle of the CMOS sensor can be determined through calibration and corrected, as presented in Fig. 3(c), yielding a measurement error that barely varies with  $\delta_\gamma$ . Moreover, Fig. 3(d) indicates the effect of a rotation,  $\delta_\alpha$  or  $\delta_\beta$ , of the CMOS sensor. A larger rotation would lead to a larger measurement error for all the three wavefronts; however, as long as we limited the rotation within the range of 0.3 mrad, the installation errors had very little effect on the measurement accuracy.

We also examined the errors attributable to the spherical wavefront calibration method. Figure 3(e) shows the measurement error distribution for plane, spherical, and freeform wavefronts. The expected error values for plane, spherical, and freeform wavefronts were 2.0, 2.1, and 2.3 nm, respectively. Figure 3(f) shows that  $\delta_\theta$  or  $\delta_\phi$  impacted measurement accuracy by causing inaccurate measurements of the relative distance of the spherical wavefronts, leading to augmented measurement error with increasing  $\delta_\theta$  or  $\delta_\phi$  values. At 20 mrad, the errors of measuring plane, spherical, and freeform wavefronts respectively, increased by 9.2%, 18.7%, and 6.4%, from their baselines. We also found that if the radius of curvature of calibrated spherical wavefronts was above 400 mm, the deviations  $\delta_x$  and  $\delta_y$  had no substantial impact on the spots' distribution as well as the calibration precision.

We built an SHWS and assessed the measurement uncertainty for the plane, spherical, and freeform wavefronts acquired in our experiments. The system parameters were consistent with those in the simulation. Via an analysis of the installation and calibration conditions of the SHWS, we evaluated the installation and calibration error distributions under the production conditions. Based on mechanical tolerances of structural components, the installation error was determined to be within  $\pm 1.71$  mrad for  $\delta_\alpha$  and  $\delta_\beta$ , with machining parallelism of 0.01 mm and effective size of 5.85 mm for MLA. The deviation gap of the MLA relative to the CMOS sensor was within 0.1 mm in the  $z$  axis direction during assembly, resulting in  $\delta_\gamma$  being within  $\pm 17.1$  mrad. We calibrated the SHWS using the spherical wavefronts calibration method.<sup>41</sup> By analyzing the calibration optical path (see the supplementary material for the analytical process), the error distribution ranges of  $\delta_x$  and  $\delta_y$  were limited to  $\pm 2$  mm, while the error ranges of  $\delta_\theta$  and  $\delta_\phi$  were set to within  $\pm 5$  mrad.

Finally, we measured several plane, spherical, and freeform wavefronts with the SHWS experimentally. The spherical wavefronts were measured from a diverging beam from an optical fiber, and plane wavefronts were obtained by collimating it. Figure 4(a) shows the measurement setup for the freeform wavefronts created by deformed optical surfaces imprinting a complicated profile in a plane wave. Figures 4(b)–4(d) illustrate the error histograms calculated from 2400 Monte Carlo simulations. When taking the value of the coverage factor  $k$  to be 2, the uncertainty of the measured plane, spherical, and freeform wavefronts was 9.66 nm ( $\lambda/65$ ), 2.43 nm

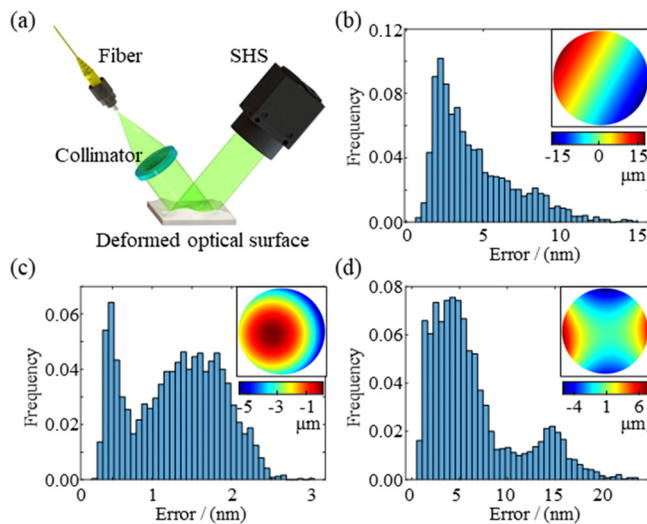


**FIG. 4.** Experiment testing the SHWS model. (a) Experimental setup for measuring freeform wavefronts with the SHWS. Histograms of the errors measured from the plane (b), spherical (c), and freeform (d) wavefronts. The insets show the corresponding wavefronts.

( $\lambda/260$ ), and 15.78 nm ( $\lambda/40$ ), respectively. From these results, we confirmed that the measured uncertainties depended on the specific form of wavefront. Among the three wavefronts, due to the SHWS utilizing spherical wavefronts calibration, and the curvature radius of the spherical wavefront shown in Fig. 4(c) being close to the range of the spherical wavefronts calibration radius, the SHWS more accurately measured the spherical wavefronts than the other two.

In conclusion, we present an uncertainty evaluation approach for the SHWS that can assess the measurement accuracy for a specific wavefront. Our approach leverages a simulation model based on the physical optics propagation and takes the installation, image acquisition, calibration, and algorithmic errors into account. Using this model, we investigated the impact of different error sources on the measurement accuracy and verified its effectiveness of using Monte Carlo methods to evaluate the uncertainty for an arbitrary wavefront. Our approach addresses the challenging problem of varying measurement accuracy encountered when the SHWS measures different wavefronts, which makes it difficult to establish a single criterion to measure their performance. By analyzing the influence of different error sources on the measurement accuracy, our method can help researchers develop their error allocation scheme during the design of sensor. Moreover, our proposed SHWS model provides a reliable and unbiased evaluation criterion for the SHWS. As our model has an end-to-end nature, it is feasible to directly evaluate the impact of improved algorithms on the final measurement accuracy of the SHWS, leading to more realistic and effective evaluation results. We hope that our work will contribute to future efforts toward enhancing the accuracy and reliability of optical measurement technologies.

See the supplementary material for details of the process of analyzing the SHWS spherical wavefronts calibration errors.

This work was sponsored by Shanghai Jiao Tong University 2030 Initiative (No. WH510363001-10), the Fundamental Research Funds for the Central Universities of Shanghai Jiao Tong University (No. AF3230004/002), the Science Foundation of Donghai Laboratory (Nos. DH-2022KF01001 and DH-2022KF01005), and the National Key Research and Development Program of China (No. 2022YFC2806600).

## AUTHOR DECLARATIONS

### Conflict of Interest

The authors have no conflicts to disclose.

## Author Contributions

Jichong Zhou and Qiaozhi He contributed equally to this work.

J.Z. and Q.H. designed the research; J.Z. wrote the codes for the numerical simulation; J.Z. and Q.H. performed the experiments; Y.Q. and D.Z. analyzed the experimental results; J.Z. and Q.H. wrote the original draft; J.Z., Z.W., and J.Y. revised the manuscript; J.Y. supervised the project. All authors contributed to the writing of the manuscript.

**Jichong Zhou:** Methodology (equal); Software (lead); Validation (lead); Writing – original draft (equal). **Qiaozhi He:** Methodology (equal); Validation (supporting); Writing – original draft (equal). **Yuan Qu:** Visualization (equal); Writing – original draft (equal); Writing – review & editing (supporting). **Dineng Zhao:** Visualization (equal); Writing – original draft (supporting). **Ziying Wu:** Writing – review & editing (supporting). **Jiamiao Yang:** Supervision (lead); Writing – review & editing (lead).

## DATA AVAILABILITY

The data that support the findings of this study are available from the corresponding author upon reasonable request.

## REFERENCES

- <sup>1</sup>J. Hernández-Delgado, Z. Malacara-Hernández, D. Malacara-Doblado, B. Vázquez-Dorrio, and D. Malacara-Hernández, *Opt. Eng.* **61**(5), 050901 (2022).
- <sup>2</sup>X. Zhang, H. Hu, D. Xue, Q. Cheng, X. Yang, W. Tang, G. Qiao, and X. Zhang, *Opt. Lasers Eng.* **161**, 107350 (2023).
- <sup>3</sup>N. Kumar, B. Pathak, R. Kesarwani, S. Goswami, A. Khare, and B. R. Boruah, *Opt. Lett.* **47**(21), 5509 (2022).
- <sup>4</sup>H. Lyu, L. Kong, S. Wang, and M. Xu, *Opt. Express* **30**(5), 7831 (2022).
- <sup>5</sup>F. G. Riesgo, S. L. S. Gómez, J. D. S. Rodríguez, C. G. Gutiérrez, Y. M. Hernando, L. M. M. Martínez, A. A. Ramos, M. C. Vera, M. N. Cagigal, and F. J. D. C. Juez, *Opt. Lasers Eng.* **158**, 107157 (2022).
- <sup>6</sup>H. Ogane, M. Akiyama, S. Oya, and Y. Ono, *Mon. Not. R. Astron. Soc.* **503**(4), 5778 (2021).
- <sup>7</sup>J. Kim, B. Fernandez, and B. Agrawal, *J. Opt. Soc. Am. A* **38**(3), 456 (2021).
- <sup>8</sup>R. W. Wilson, *Mon. Not. R. Astron. Soc.* **337**(1), 103 (2002).
- <sup>9</sup>E. M. Seromenho, A. Marmin, S. Facca, N. Bahloul, S. Perrin, and A. Nahas, *Appl. Phys. Lett.* **121**(11), 113702 (2022).
- <sup>10</sup>Y. Liu, C. Ma, Y. Shen, J. Shi, and L. V. Wang, *Optica* **4**(2), 280 (2017).
- <sup>11</sup>C. T. Holló, M. Kurucz, A. Csorba, K. Kránitz, I. Kovács, Z. Z. Nagy, and G. Erdei, *Sci. Rep.* **10**(1), 12585 (2020).
- <sup>12</sup>S. Koh, R. Inoue, Y. Iwamoto, T. Mihashi, T. Soma, N. Maeda, and K. Nishida, *Eye Contact Lens* **49**(3), 98 (2023).
- <sup>13</sup>M. Vacalebre, R. Frison, C. Corsaro, F. Neri, S. Conoci, E. Anastasi, M. C. Curatolo, and E. Fazio, *Polymers* **14**(23), 5321 (2022).
- <sup>14</sup>Z. Cheng, D. Liu, and L. Zhang, *Appl. Phys. Lett.* **115**(12), 121107 (2019).

- <sup>15</sup>X. Zhu, L. Lian, P. Yang, Z. Chang, X. Huang, X. Wang, Z. Yu, and P. Zhang, *Opt. Lett.* **48**(2), 211 (2023).
- <sup>16</sup>F. Zhang, Y. Liu, W. Wang, L. Geng, and Z. Xiao, *Appl. Opt.* **62**(12), 2988 (2023).
- <sup>17</sup>G. Baffou, *ACS Photonics* **10**(2), 322 (2023).
- <sup>18</sup>D. Wang, C. Wang, X. Tian, H. Wu, J. Liang, and R. Liang, *Opt. Lasers Eng.* **128**, 106032 (2020).
- <sup>19</sup>L. A. Alemán-Castaneda, B. Piccirillo, E. Santamato, L. Marrucci, and M. A. Alonso, *Optica* **6**(4), 396 (2019).
- <sup>20</sup>D. Zheng, Z. Ma, Z. Zhang, and C. Hu, *Appl. Opt.* **62**(3), 745 (2023).
- <sup>21</sup>D. Wang, Y. Yang, C. Chen, and Y. Zhuo, *Appl. Opt.* **50**(16), 2342 (2011).
- <sup>22</sup>Y. Du, G. Feng, H. Li, J. Vargas, and S. Zhou, *Opt. Lett.* **37**(19), 3927 (2012).
- <sup>23</sup>B. Platt and R. V. Shack, *J. Refractive Surg.* **17**(5), S573 (2001).
- <sup>24</sup>R. Lane and M. Tallon, *Appl. Opt.* **31**(32), 6902 (1992).
- <sup>25</sup>See <https://www.imagine-optic.com/products/haso4-broadband-wavefront-sensor/> for “Detailed Specs” (last accessed June 6, 2023).
- <sup>26</sup>J. Pfund, N. Lindlein, and J. Schwider, *Appl. Opt.* **37**(1), 22 (1998).
- <sup>27</sup>J. Vargas, L. Gonzalez-Fernandez, J. A. Quiroga, and T. Belenguer, *Opt. Lett.* **35**(11), 1762 (2010).
- <sup>28</sup>D. Neal, J. Copland, and D. Neal, “Shack-Hartmann wavefront sensor precision and accuracy,” *Proc. SPIE* **4779**, 148 (2002).
- <sup>29</sup>H. Li, H. Song, C. Rao, and X. Rao, *Opt. Commun.* **281**(4), 750 (2008).
- <sup>30</sup>C. Li, H. Xian, W. Jiang, and C. Rao, *Topics in Adaptive Optics* (IntechOpen, 2012).
- <sup>31</sup>S. Thomas, T. Fusco, A. Tokovinin, M. Nicolle, V. Michau, and G. Rousset, *Mon. Not. R. Astron. Soc.* **371**(1), 323 (2006).
- <sup>32</sup>C.-M. Chia, K.-Y. Huang, and E. Chang, *Opt. Eng.* **55**(1), 013105 (2016).
- <sup>33</sup>V. Akondi, S. Steven, and A. Dubra, *Opt. Lett.* **44**(17), 4167 (2019).
- <sup>34</sup>P. Wei, X. Li, X. Luo, and J. Li, *Opt. Eng.* **59**(4), 043103 (2020).
- <sup>35</sup>B. Pathak and B. R. Boruah, *J. Opt. Soc. Am. A* **34**(12), 2194 (2017).
- <sup>36</sup>B. Pathak and B. R. Boruah, *J. Opt.* **16**(5), 055403 (2014).
- <sup>37</sup>L. Huang and A. Asundi, *Appl. Opt.* **51**(31), 7459 (2012).
- <sup>38</sup>L. Huang, J. Xue, B. Gao, C. Zuo, and M. Idir, *Opt. Lasers Eng.* **91**, 221 (2017).
- <sup>39</sup>M. Aftab, H. Choi, R. Liang, and D. W. Kim, *Opt. Express* **26**(26), 34428 (2018).
- <sup>40</sup>J. Yang, L. Wei, H. Chen, X. Rao, and C. Rao, *Opt. Commun.* **283**(6), 910 (2010).
- <sup>41</sup>A. Chernyshov, U. Sterr, F. Riehle, J. Helmcke, and J. Pfund, *Appl. Opt.* **44**(30), 6419 (2005).
- <sup>42</sup>J. W. Goodman, *Introduction to Fourier Optics* (Roberts and Company Publishers, 2005), p. 98.
- <sup>43</sup>K. Matsushima, H. Schimmel, and F. Wyrowski, *J. Opt. Soc. Am. A* **20**(9), 1755 (2003).